Click Here
for
Full
Article

Magnetospheric configurations from a high-resolution data-based magnetic field model

N. A. Tsyganenko[1] and M. I. Sitnov[2]

[1] We present first results of the magnetospheric magnetic field modeling, based on large sets of spacecraft data and a high-resolution expansion for the field of equatorial currents. In this approach, the field is expanded into a sum of orthogonal basis functions of different scales, capable to reproduce arbitrary radial and azimuthal variations of the geomagnetic field, including its noon-midnight and dawn-dusk asymmetries. Combined with the existing method to model the global field of Birkeland currents, the new approach offers a natural way to consistently represent the field of both the tail and symmetrical/partial ring currents. The proposed technique is particularly effective in the modeling of the inner magnetosphere, a stumbling block for the first-principle approaches. The new model has been fitted to various subsets of data from Geotail, Polar, Cluster, IMP-8, and GOES-8, GOES-9, GOES-10, and GOES-12 spacecraft, corresponding to different activity levels, solar wind IMF conditions, and storm phases. The obtained maps of the magnetic field reproduce most basic features of the magnetospheric structure, their dependence on the geomagnetic activity and interplanetary conditions, as well as characteristic changes associated with the main and recovery phases of magnetic storms.

1. Introduction

[2] The ultimate goal of empirical modeling is to extract maximum meaningful information on the modeled object from a given body of data. In most situations, the amount of that information critically depends on the coverage of the object by the data in space and time. Sparse and/or nonuniform coverage allows one to use rather simple models with a few degrees of freedom, replicating only some basic features of the object and its response to external input. In the specific case of the Earth's magnetosphere, the lack of in situ spacecraft data as well as the shortage of continuous concurrent data from solar wind monitors in 1970–1980s was the main factor that limited the resolution of early models, constructed from a few "custom-made" modules representing contributions from major magnetospheric current systems (see *Tsyganenko* [1990] for a review). The situation has changed dramatically since then: during the last decade the magnetospheric data pool was greatly expanded owing to almost continuous monitoring of the solar wind and interplanetary magnetic field (IMF) by WIND, ACE, and IMP-8, a very dense coverage of the near-equatorial magnetosphere at $10 < R < 30 \, R_E$ by nearly 14 years worth of Geotail data, and large amounts of

low- and high-latitude data from GOES-8, GOES-9, GOES-10, GOES-12, and Polar satellites. Such a wealth of data offered an attractive opportunity to study in much more detail the magnetospheric structure and its response to external conditions.

[3] Most of the electric current associated with the observed configuration of the distant geomagnetic field concentrates at low latitudes, where the plasma beta parameter rises to its maximal values. From the modeling perspective, these currents can be viewed as a single large-scale equatorial system, including the ring current in the inner magnetosphere and the cross-tail current sheet at larger distances. The second major component, substantially different from the first one, is the system of field-aligned currents (FAC), including those associated with the storm-time partial ring current (PRC). Their essential role is to directly transfer the solar wind momentum from the magnetosheath to the high-latitude ionosphere (Region 1 FAC) and to divert the equatorial currents to higher latitudes, providing the electrodynamical coupling of the plasma sheet with the auroral zone (Region 2 FAC and the PRC). The third component is the magnetopause current system, whose role is to confine the total field within the magnetospheric boundary.

[4] In this work we develop a new approach to consistently unify all the three groups of sources into a single model and demonstrate its feasibility by deriving from data sample geomagnetic configurations, corresponding to different conditions in the solar wind and in the magnetosphere. The following sections 2 and 3 describe the details of the new approximation for the field of equatorial and field-aligned

---

[1]Universities Space Research Association and Space Weather Laboratory, NASA Goddard Space Flight Center, Greenbelt, MD, USA.
[2]Institute for Research in Electronics and Applied Physics, University of Maryland, College Park, MD, USA.

currents, section 4 overviews the data used in this study, section 5 addresses important new elements in the derivation of the model field from the data. Section 6 presents the main results and their discussion, and section 7 summarizes the work.

2. Modeling Equatorial Current System

[5] In the recent models [*Tsyganenko*, 1995, 1996, 2002a, 2002b; *Tsyganenko et al.*, 2003; *Tsyganenko and Sitnov*, 2005, referred henceforth as T96, T02a, b, TSK03, and TS05, respectively] the tail field was represented by a linear combination of two or three partial fields, or "modules" $\mathbf{B}_{T,i}$ ($i = 1, 2, 3$), corresponding to contributions from disk-like current sheets with largely different spatial scales. Each partial field was separately confined inside a model magnetopause by adding to the field of the current sheet a curl-free "shielding" field, which eliminated the normal component of the total field on the magnetopause. As explained in more detail by *Sotirelis et al.* [1994], that procedure is equivalent to diverting and closing the originally unbounded currents over the magnetopause. Being relatively simple and straightforward, the approach was at the same time inherently limited. First, using the axially symmetric disks excludes from the outset any dawn-dusk asymmetry of the tail current. Even though the observed midtail field was found basically symmetric with respect to the midnight plane [e.g., *Fairfield*, 1986], one cannot rule out asymmetries at closer distances, especially in the inner tail and near the dawn-dusk flanks of the magnetosphere, in view of significant asymmetries in the measured particle fluxes [e.g., *Stubbs et al.*, 2001]. Second, at radial distances larger than $R \sim 5\ R_E$ the equatorial current becomes significantly asymmetric between noon and midnight: on the nightside the current is rather strong and concentrates within a relatively thin sheet, while on the dayside it is much weaker and more spread out in latitude. In the above cited models that kind of asymmetry was taken into account by introducing a variable thickness of the current sheet as a function of X and by requiring that the current had a steep inner edge at $R \sim 10\ R_E$, with virtually no current at smaller distances. In the T02 and TS05 models, the equatorial currents were also allowed to shift along the x axis within a limited range, in response to varying degree of disturbance. That added some more flexibility, but the overall geometry of the tail current remained rigidly prescribed by the above a priori assumptions.

[6] The goal of the present work is to lift most of the limitations of the previous models by using a completely different approach. Instead of approximating the tail field by a few custom-made modules, we represent it by a series of orthogonal basis functions, each one shielded within a common model magnetopause. As shown below, simply by adding more terms in the expansion, one can set the model's resolution at any desired level (of course, commensurate with the available data coverage). The model easily takes into account the dawn-dusk and noon-midnight asymmetries of the tail currents and couples them with the three-dimensional system of FAC. Moreover, the new method makes it possible to naturally include in the model the fields of the inner magnetospheric sources, such as the symmetric

(SRC) and partial (PRC) ring currents. This eliminates the need for sophisticated ad hoc approximations for those fields [*Tsyganenko*, 2000a] used in T02, TSK03, and TS05 models, and makes our empirical approach more consistent.

2.1. Approach

[7] Consider a planar current sheet in a cylindrical coordinate system $\{\rho, \phi, z\}$ with the z axis normal to the equatorial plane. The basic idea is to obtain general solutions of the Ampere's equation

$$\nabla \times \mathbf{B} = (4\pi/c)\left[j_\rho(\rho,\phi)\mathbf{e}_\rho + j_\phi(\rho,\phi)\mathbf{e}_\phi\right]\delta(z) \qquad (1)$$

above and below the plane $z = 0$ and use them for matching the magnetic field of an arbitrary distribution of the equatorial current. One might seek a direct solution of equation (1) from the very beginning in terms of a vector potential $\mathbf{A}(\rho, \phi, z)$. Unfortunately, that can only be realized for axially symmetric configurations with a purely azimuthal current $\mathbf{j} = j(\rho)\ \delta(z)\ \mathbf{e}_\phi$. In that case the vector potential can also be assumed purely azimuthal, $\mathbf{A} = A(\rho, z)\ \mathbf{e}_\phi$, and the resultant scalar equation for $A(\rho,z)$ can be solved by separating variables [*Tsyganenko*, 1989; *Tsyganenko and Peredo*, 1994; referred henceforth as T89 and TP94, respectively]. As shown below, derivation of the vector potential in the general case is more involved; yet it is very important, because it will enable us to further generalize the model, taking into account the finite thickness of the current sheet and its variation across the tail.

[8] We obtain the desired solution in three steps. First, the Ampere's equation (1) is reduced to Laplace's equation for scalar potentials γ^+ and γ^- above and below the equatorial plane, determining there the curl-free magnetic field $\mathbf{B} = -\nabla\gamma^\pm$. Then the corresponding vector potential is derived from the scalar one, using a transformation by *Stern* [1987]. Finally, the obtained solution is modified, so that the originally infinitely thin current sheet spreads out in the Z direction over a finite thickness.

[9] The obtained magnetic field corresponds to an equatorial distribution of the current, infinitely extended in the X and Y directions, while in actuality those currents are spatially bounded, and the corresponding magnetic field is also confined within the magnetopause. As in the earlier models, we take this into account by adding a curl-free shielding field, whose configuration is determined to minimize the RMS normal component $\langle B_n^2\rangle^{1/2}$ of the total field at the boundary. One more modification is then carried out, to include in the model the deformation of the tail current sheet due to seasonal and diurnal changes in the orientation of the Earth's dipole axis, as well as its twisting during intervals with large azimuthal component of the IMF. More details on these procedures are given below.

2.2. Derivation of Vector Potentials

[10] For any distribution of currents in the equatorial plane, the magnetic field $\mathbf{B}$ outside that plane is both curl-free and divergenceless and, hence, can be represented by the gradient of a scalar potential γ, satisfying Laplace's equation. The potentials γ^+ and γ^-, corresponding to the

northern ($0 < z < +\infty$) and southern ($-\infty < z < 0$) halfspace, respectively, can be represented by a spectrum of cylindrical harmonics $\gamma_m^\pm(k, \rho, \phi, z)$, so that

$$\gamma^\pm(\rho, \phi, z) = \sum_{m=0}^{\infty} \int_0^\infty dk \, a_m(k) \, \gamma_m^\pm(k, \rho, \phi, z) \qquad (2)$$

where $a_m(k)$ is a set of amplitude functions with the discrete azimuthal and continuous radial wave numbers m and k, respectively, and [e.g., *Moon and Spencer*, 1971]

$$\gamma_m^\pm(k, \rho, \phi, z) = \pm J_m(k\rho) \left\{ \begin{array}{c} \cos(m\phi) \\ \sin(m\phi) \end{array} \right\} \exp(-k|z|) \qquad (3)$$

in which J_m are Bessel functions of the mth order. The sign factor in equation (3) ensures the continuity of the normal magnetic field component B_z across the plane $z = 0$, required by $\nabla \cdot \mathbf{B} = 0$. The tangential component of the magnetic field has a jump $\Delta \mathbf{B}_t$ across the equatorial plane, related to the corresponding surface density $\mathbf{J}$ of the equatorial current by $\mathbf{J} = (c/4\pi) (\mathbf{e}_z \times \Delta \mathbf{B}_t)$.

[11] According to *Stern* [1987], in cylindrical coordinates the transition from scalar to vector potentials can be done using the transformation

$$\mathbf{A} = \rho^2 \nabla\Psi \times \nabla\phi \qquad (4)$$

where the generating function Ψ is related to the scalar potential γ by the equation

$$\gamma = -\partial\Psi/\partial\phi \qquad (5)$$

A generating function Ψ_m satisfying equations (3) and (5) can be taken in the form

$$\Psi_m^\pm = \pm \frac{J_m(k\rho)}{m} \left\{ \begin{array}{c} \sin(m\phi) \\ \cos(m\phi) \end{array} \right\} \exp(-k|z|) \qquad (6)$$

Then the corresponding vector potential reads

$$\mathbf{A}_m(k, \rho, \phi, z) = -\frac{k\rho}{m} \left[J_m(k\rho)\mathbf{e}_\rho + \mathrm{sign}(z)J_m'(k\rho)\mathbf{e}_z \right] \left\{ \begin{array}{c} \sin(m\phi) \\ \cos(m\phi) \end{array} \right\}$$
$$\cdot \exp(-k|z|) \qquad (7)$$

Note that the above derivation of the vector potential is valid only for the case of axially asymmetric fields with $m = 1, 2, \ldots$. The axisymmetric case $m = 0$ must be treated separately, and there exist two seemingly equivalent solutions. The first one can be derived using the same procedure: start from the scalar potential $\gamma_0^\pm = \pm J_0(k\rho) \exp(-k|z|)$ and obtain a generating function (in this case, just by multiplying $\gamma_0^\pm$ by $-\phi$), which yields the vector potential as

$$\mathbf{A}_0(k, \rho, \phi, z) = -k\phi\rho \exp(-k|z|) \left[J_0(k\rho)\mathbf{e}_\rho + \mathrm{sign}(z)J_0'(k\rho)\mathbf{e}_z \right] \qquad (8)$$

The second solution is a purely azimuthal vector potential, derived in T89 and TP94:

$$\mathbf{A}_0(k, \rho, z) = J_1(k\rho) \exp(-k|z|)\mathbf{e}_\phi \qquad (9)$$

By taking curls of equations (8) and (9) one can verify that these two potentials are equivalent, that is, yield identical magnetic fields. This equivalence extends to a more general case of a current sheet with a finite (but constant) thickness, but it fails as we further generalize the solution by allowing the thickness to vary with X and Y (more details below). In that case, the components of $\mathbf{B}$ generated by the potential equation (8) acquire terms proportional to the azimuthal angle and, hence, become nonperiodic functions of ϕ, which is unacceptable. The second solution equation (9) remains well behaved in that sense and, hence, it was chosen to represent the axisymmetric part of our model field.

[12] Now we generalize the obtained vector potentials by taking into account the finite thickness of the current sheet. This is easily achieved by replacing $|z|$ and $\mathrm{sign}(z)$ with $\zeta = \sqrt{z^2 + D^2}$ and z/ζ, respectively, which broadens the initially delta-like profile of the current density. Moreover, the half-thickness scale D can be allowed to vary across the tail, $D = D(\rho, \phi)$. With these modifications, the vector potentials take the form

$$\mathbf{A}_0(k, \rho, z) = J_1(k\rho) \exp(-k\zeta)\mathbf{e}_\phi \qquad (10)$$

$$\mathbf{A}_m(k, \rho, \phi, z) = -\frac{k\rho}{m} \left[J_m(k\rho)\mathbf{e}_\rho + \frac{z}{\zeta}J_m'(k\rho)\mathbf{e}_z \right]$$
$$\cdot \left\{ \begin{array}{c} \sin(m\phi) \\ \cos(m\phi) \end{array} \right\} \exp(-k\zeta) \qquad (11)$$

Returning to the general expansion for an arbitrary distribution of the equatorial current, we now replace equation (2) with

$$\mathbf{A}(\rho, \phi, z) = \sum_{m=0}^{\infty} \int_0^\infty dk \, a_m(k) \, \mathbf{A}_m(k, \rho, \phi, z) \qquad (12)$$

where the "partial" vector potentials $\mathbf{A}_m$ are given by equations (10) and (11).

[13] A novel feature of this work is that we expand the tail field model beyond the first term in equation (12) with $m = 0$, that is, introduce a plethora of azimuthally asymmetric elementary current sheets with $m \neq 0$. This makes it possible to approximate with any desired resolution the magnetic field due to any distribution of the equatorial current. In this regard, note that all the earlier models (T89, T96, T02, and TS05) used special forms of the amplitude function $a_0(k)$, which yielded smooth radial distributions of the magnetotail current $J(R)$, with a single peak at $R \sim 10 \, R_E$ and a gradual tailward decrease beyond that distance. That approach resulted in computationally simple codes; however, it also restricted the models' scope to a limited class of a priori prescribed distributions of the tail field. In this work we abandon most of the previous ad hoc assumptions and leave it entirely to the model and data to establish the actual structure of the magnetic field. To that

end, we replace in equation (12) the integration over a continuous spectrum $a_m(k)$ by a discrete summation over an equidistant set of wave numbers k_n:

$$\mathbf{A}(\rho, \phi, z) = \sum_{n=1}^{N} a_{0n}\, \mathbf{A}_0(k_n, \rho, z) + \sum_{m=1}^{M} \sum_{n=1}^{N} a_{mn}\, \mathbf{A}_m(k_n, \rho, \phi, z)$$

(13)

where the axisymmetric part of the vector potential is singled out into a separate sum, and $k_n = n/\rho_0$ where ρ_0 is a radial scale, corresponding to the largest wavelength in the expansion of the potential into the series of finite elements. By the order of magnitude, its value should correspond to the spatial extent of the modeling region; in the present work we chose $\rho_0 = 20\ R_E$. The upper limits of the summation, N and M, define the radial and the angular (azimuthal) resolution of the model, respectively. Their optimal choice translates into a trade-off between the computational efficiency of the model and the available degree of detail, which critically depends on the coverage of the modeled region by the data. A more extensive discussion of these issues will be made in sections 4 and 5 below.

2.3. Magnetic Field Components

[14] The expansion (13) for the vector potential generates a corresponding expansion for the magnetic field vector, in which the first (axisymmetric) sum will be designated by the superscript s (standing for "symmetric"). The second sum will be further divided into two parts. The first part corresponds to choosing the factor $\sin(m\phi)$ in the right-hand side of equation (11), and we will call it the "odd" mode (designated by the superscript o), since in this case both components of $\mathbf{A}$ are odd functions of the coordinate y. The second part will be termed the "even" mode (hence, e). With all these notations, we now have

$$\mathbf{B}(\rho, \phi, z) = \sum_{n=1}^{N} a_n^{(s)} \mathbf{B}_n^{(s)} + \sum_{m=1}^{M} \sum_{n=1}^{N} a_{mn}^{(o)} \mathbf{B}_{mn}^{(o)} + \sum_{m=1}^{M} \sum_{n=1}^{N} a_{mn}^{(e)} \mathbf{B}_{mn}^{(e)}$$

(14)

where

$$B_{n,\rho}^{(s)} = k_n J_1(k_n\rho)\,(z/\zeta)\,\exp(-k_n\zeta)$$

$$B_{n,\phi}^{(s)} = 0$$

(15)

$$B_{n,z}^{(s)} = k_n \exp(-k_n\zeta)\left[J_0(k_n\rho) - \frac{D}{\zeta}\frac{\partial D}{\partial \rho} J_1(k_n\rho)\right]$$

$$B_{mn,\rho}^{(o)} = -\frac{k_n z}{\zeta} J_m'(k_n\rho)\exp(-k_n\zeta)$$

$$\cdot \left[\cos(m\phi) - \frac{D}{m\zeta}\frac{\partial D}{\partial \phi}\left(k_n + \frac{1}{\zeta}\right)\sin(m\phi)\right]$$

$$B_{mn,\phi}^{(o)} = \frac{k_n z}{\zeta}\exp(-k_n\zeta)\left[\frac{m}{k_n\rho}J_m(k_n\rho)\right.$$

(16)

$$\left. - \frac{\rho D}{m\zeta}\frac{\partial D}{\partial \rho}\left(k_n + \frac{1}{\zeta}\right)J_m'(k_n\rho)\right]\sin(m\phi)$$

$$B_{mn,z}^{(o)} = k_n J_m(k_n\rho)\exp(-k_n\zeta)\left[\cos(m\phi) - \frac{k_n D}{m\zeta}\frac{\partial D}{\partial \phi}\sin(m\phi)\right]$$

$$B_{mn,\rho}^{(e)} = -\frac{k_n z}{\zeta} J_m'(k_n\rho)\exp(-k_n\zeta)$$

$$\cdot \left[\sin(m\phi) + \frac{D}{m\zeta}\frac{\partial D}{\partial \phi}\left(k_n + \frac{1}{\zeta}\right)\cos(m\phi)\right]$$

$$B_{mn,\phi}^{(e)} = -\frac{k_n z}{\zeta}\exp(-k_n\zeta)\left[\frac{m}{k_n\rho}J_m(k_n\rho)\right.$$

(17)

$$\left. - \frac{\rho D}{m\zeta}\frac{\partial D}{\partial \rho}\left(k_n + \frac{1}{\zeta}\right)J_m'(k_n\rho)\right]\cos(m\phi)$$

$$B_{mn,z}^{(e)} = k_n J_m(k_n\rho)\exp(-k_n\zeta)\left[\sin(m\phi) + \frac{k_n D}{m\zeta}\frac{\partial D}{\partial \phi}\cos(m\phi)\right]$$

[15] Equations for the corresponding components B_ρ, B_ϕ, and B_z of the magnetic field include spatial derivatives of the half-thickness $D(\rho, \phi)$ of the current sheet, whose explicit form will be described in the next section 2.4. Also note that the expansion (14) does not include the shielding field; that issue will be addressed in section 2.5.

[16] The structure of the model field can be better visualized by plotting families of flow lines of the corresponding electric current $\mathbf{j} = \nabla \times \mathbf{B}$, for various values of wave numbers k_n and azimuthal harmonic orders m. Figure 1 displays four sample plots, from a large-scale symmetric current disk ($m = 0$, $k = 0.1$, top, left) to a higher-order ($m = 2$) smaller-scale ($k = 0.3$) element with an o-type symmetry (bottom, right). The plots were obtained assuming a constant thickness of the current sheet $D = 2\ R_E$. Using a linear combination of a sufficiently large number of such elements allows one to approximate the magnetic field for any distribution of the equatorial current.

2.4. Spatial Variation of the Current Sheet Thickness

[17] Assuming a constant half-thickness D of the equatorial current sheet is only a crude approximation. In the distant tail, the plasma sheet is quite variable and turbulent, so that the local current sheet thickness can vary within a wide range, resulting in larger values of D. At closer distances, owing to the rapidly increasing dipole field one may expect a more regular structure of the equatorial current, concentrated within a limited range of latitudes around the dipole equator, where the magnetic field magnitude is minimal. Therefore in the inner magnetosphere the current sheet thickness, on the order of magnitude, does not exceed a fraction of the corresponding L-parameter and, hence, should decrease with decreasing geocentric distance. On the other hand, as was found in all previous empirical modeling studies [T87 and later models], the tail current sheet expands in the Y-direction toward its dawn-dusk flanks. Finally, due to a generally compressed magnetic field on the dayside, equatorial currents in that region are expected to spread over a larger interval of latitudes than on the nightside, implying larger values of D there.

[18] The above features can be taken into account by a straightforward modification of the model, in which the parameter D is assumed as a simple analytical function of position on the equatorial plane. In this study we chose it in the following form

$$D = D_0\left[1 - f(\epsilon)\frac{\rho_D^2}{\rho_D^2 + \rho^2}\right]\left[1 + \alpha\exp(X/10)\right]\exp\left[\beta(Y/20)^2\right]$$
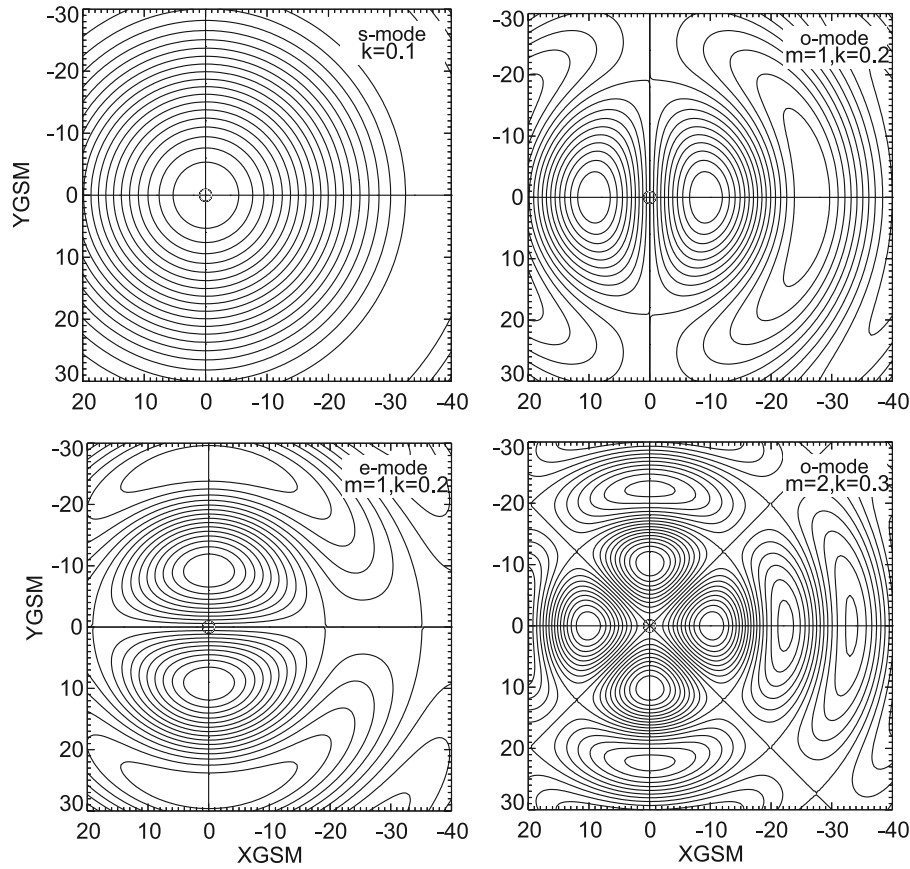
(18)

Figure 1. Sample configurations of the equatorial electric current flow lines, corresponding to four harmonics of the vector potential equations (10) and (11).

where D_0 is the asymptotic half-thickness of the current sheet in the center of the distant tail, f is the magnitude of the sheet thinning in the inner magnetosphere, $\rho_D = 5\ R_E$, and the coefficients α and β define the rate of the current sheet expansion in the sunward and dawn-dusk directions, respectively. To avoid negative values of D, the coefficient f was intentionally taken in the form $f(\varepsilon) = 0.5\ (1 + \tanh(\varepsilon))$, so that $|f(\varepsilon)| < 1$ for any value of the variable parameter ε. In total, the form equation (18) includes four variable parameters.

2.5. Approximations for the Shielding Field

[19] As in the earlier works (T96 and more recent models), our approach is to define and add a corresponding shielding field $\mathbf{B}_{sh}$ to each of the individual modules $\mathbf{B}_n^{(s)}$, $\mathbf{B}_{mn}^{(o)}$, and $\mathbf{B}_{mn}^{(e)}$ in equation (14), so that the final expansion for the total field of equatorial currents becomes

$$\mathbf{B}_{eq} = \sum_{n=1}^{N} a_n^{(s)} \left(\mathbf{B}_n^{(s)} + \mathbf{B}_{sh,\,n}^{(s)} \right) + \sum_{m=1}^{M} \sum_{n=1}^{N} a_{mn}^{(o)} \left(\mathbf{B}_{mn}^{(o)} + \mathbf{B}_{sh,\,mn}^{(o)} \right)$$
$$+ \sum_{m=1}^{M} \sum_{n=1}^{N} a_{mn}^{(e)} \left(\mathbf{B}_{mn}^{(e)} + \mathbf{B}_{sh,\,mn}^{(e)} \right) \qquad (19)$$

This ensures a full confinement of the total field inside the magnetopause, regardless of specific values of the amplitude coefficients $a_n^{(s)}$, $a_{mn}^{(o)}$, and $a_{mn}^{(e)}$ in the expansion. A great advantage of this approach is that it allows to define $\mathbf{B}_{sh,\,n}^{(s)}$,

$\mathbf{B}_{sh,\,mn}^{(o)}$, and $\mathbf{B}_{sh,\,mn}^{(e)}$ only once, after which the model can be fitted to any set of data by varying the coefficients, but without recalculating the shielding fields.

[20] Since the shielding currents flow at the magnetopause, their field inside the magnetosphere can be described using a scalar potential. In particular, the shielding fields $\mathbf{B}_{sh}^{(s,o,e)}$ for each term in equation (19) can be constructed using expansions in cylindrical harmonics similar to equation (3)

$$U = \sum_{k=1}^{K} \sum_{l=0}^{L} c_{kl} J_l(\kappa_k \rho) \begin{Bmatrix} \cos(l\phi) \\ \sin(l\phi) \end{Bmatrix} \sinh(\kappa_k z) \qquad (20)$$

where the factor $\cos(l\phi)$ corresponds to the terms having the s-symmetry and o-symmetry, and $\sin(l\phi)$ enters in the e-terms. The summation limits K and L were chosen equal to 5 and 15, respectively, to provide a reasonable tradeoff between the relative RMS error (on the order of $7-10\%$) and the length of expansions (hence, computation time). Expansions for individual magnetic field components can be obtained by taking the gradient of equation (20) and are similar in their structure to equations (15), (16), and (17); we do not reproduce them for the sake of brevity.

[21] Figure 2 illustrates the effect of the shielding by showing sample distributions of the normal component B_n of the unshielded field on the model magnetopause (left panel), taken with the opposite sign, and the corresponding normal component $B_{sh\,n}$ of the shielding field (right panel) for the term with $m = 4$ and $n = 3$ in the second double sum
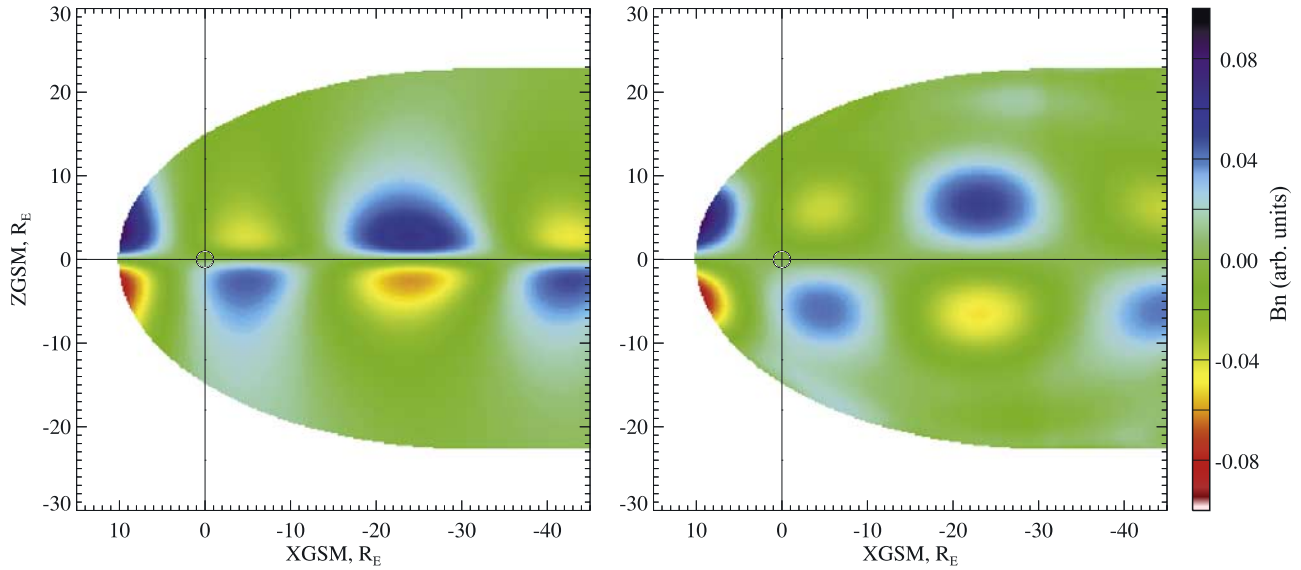
Figure 2. Distribution on the magnetopause of the normal component of the unshielded field of the equatorial current sheet with the *o*-type symmetry in equation (14) ($n = 3$ and $m = 4$; left panel), to be compared with the corresponding distribution of the best fit shielding field, approximated using the scalar potential equation (20) (right).

in equation (18). In an ideal case of a perfect shielding, $B_n + B_{sh\ n} = 0$, and the two distributions would be identical. Using the finite expansion (19), however, limits the accuracy and, even though the overall agreement is satisfactory, both negative (red) and positive (blue) peaks of $B_{sh\ n}$ are located somewhat farther from the equatorial plane than those in the unshielded field distribution. This discrepancy can be reduced by adding more terms in the expansion (19) and thus increasing its flexibility near the flanks of the current sheet, where the magnetic field rapidly reverses its orientation across the equatorial plane.

3. Contribution From Field-Aligned Currents

[22] Modeling of the field $\mathbf{B}_{FAC}$ of field-aligned currents essentially relies in this work on the approach developed earlier in T02a; here we only briefly reiterate the basic steps of the model derivation, and the reader is referred to the above cited work for details. Both Region 1 and Region 2 field-aligned currents were assumed to flow into and out of the ionosphere along closed contours encircling the polar cap, so that in each case the current flow lines are confined to analytically defined surfaces, S_1 or S_2, respectively. At low altitudes, the shape of each surface approximately matches the diverging dipolar field lines, but then gradually stretches out at larger radial distances. The strength of the upward/downward currents was defined as a simple sinusoidal function of the foot point solar-magnetic longitude ϕ. For each current system, the corresponding magnetic field $\mathbf{B}_{FAC}$ was first calculated numerically at a grid of points covering a wide range of distances, by means of a Biot-Savart integration. The next step was to derive a suitable analytical model, yielding the best fit to the numerically obtained set of field vectors. As a convenient zero-order approximation $\mathbf{B}_{FAC}^{(0)}$ we chose the "conical" harmonics [*Tsyganenko*, 1991], corresponding to purely radial currents that flow within a

conical sheet S_c of finite thickness, with the current density varying with the longitude as $\sin m\phi$ ($m = 1, 2, \ldots$). These harmonics will be called below "antisymmetric", because in this case the field-aligned currents at dawn and dusk have the same magnitude but opposite directions, e.g., downward at dawn and upward at dusk. Since the shape of the conical current sheets grossly differs from that of the surfaces S_1 and S_2, the corresponding zero-order magnetic field $\mathbf{B}_{FAC}^{(0)}$ is also different from the numerically computed $\mathbf{B}_{FAC}$. To bring them into closer agreement, the zero-order field $\mathbf{B}_{FAC}^{(0)}$ was modified by applying a flexible deformation of space in spherical coordinates $\mathbf{R} \Rightarrow \mathbf{R}^*$. The deformation parameters were found by minimizing the rms difference between the numerically computed field $\mathbf{B}_{FAC}$ and its analytical approximation $\mathbf{B}'_{FAC}$, obtained by deforming the conical field as

$$\mathbf{B}'_{FAC} = \hat{\mathbf{T}}\,\mathbf{B}_{FAC}^{(0)}(\mathbf{R}^*) \qquad (21)$$

where $\hat{\mathbf{T}}$ is the deformation tensor [*Tsyganenko*, 1998, equation (6)]. The best fit deformation yielded the desired analytical approximation for the field $\mathbf{B}_{FAC}$ and transformed the original conical current sheet S_c into a modified surface, close to that used in the numerical computation (that is, either S_1 or S_2).

[23] As was already discussed in T02 (section 2.3.1), the Region 2 currents and the partial ring current should be viewed as a single current system because they are driven by the same physical mechanism (that is, sunward plasma convection in the inner tail) and are located in the same region. In the T02 model, however, for the sake of mathematical tractability they were treated as separate sources, so that the model PRC represented the innermost part of the system confined within $R \sim 5\ R_E$, while the model Region 2 currents extended to larger distances and blended there with the cross-tail current. That artificial separation was dictated
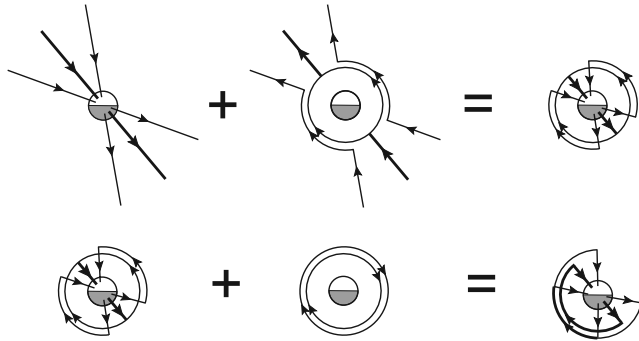
Figure 3. Schematic illustration of the Region 2 FAC and PRC current systems, obtained by combining the deformed conical model of T02 with the flexible equatorial currents, corresponding to equation (14). Top: the conical T02 FACs (left) are diverted by adding a system of equatorial currents (center), which results in a two-loop ("quadrupole") three-dimensional current system, localized at closer geocentric distances (right). Bottom: adding an axisymmetric ring current (center) to the above system converts it into a partial ring current, peaked in the evening sector (right).

by an inherent deficiency of the model of deformed conical currents, namely, by the lack of the azimuthal component of **j**, needed to close them in the plasma sheet.

[24] The present approach offers a natural way to include the closure currents at low latitudes, and thus eliminates the need in a separate PRC module. Figure 3 qualitatively explains the idea: its essence is to divert in the azimuthal direction the radial component of the model FAC in the plasma sheet, merely by adding a suitable distribution of equatorial currents. As a first step (Figure 3, top), we add a distribution with oppositely directed radial currents, which cancels the original currents at large distances and thus confines them to the inner magnetosphere as a two-loop three-dimensional system, termed in an earlier work as a "quadrupole" current [*Tsyganenko*, 2000a]. Adding then a suitably distributed axisymmetric ring current (Figure 3, bottom) weakens the eastward current on the morning side, but strengthens the westward current in the evening sector, which results in a typical PRC configuration. Note that the above scheme just illustrates the principle: in fact, there is no need to add any more special terms into the model, because the expansion (14) for the field of equatorial currents, due to its great flexibility will automatically include the effect of the closure currents for the FAC system, merely by a proper adjustment of its coefficients. Also, note that the model allows us to easily reproduce the dawn-dusk asymmetry of the FAC/PRC system, an inherent feature of the storm-time magnetosphere. To that end, we introduce a "symmetric" component in the FAC system, in which the downward currents are localized around noon and upward currents near midnight. Although such a possibility was briefly discussed in T02a, the symmetric FAC was not included in the T02 model; instead, the PRC was allowed to rotate around the solar-magnetic z axis and thus replicate the duskside storm-time depression of the geomagnetic field. In the present model we do not have a separate PRC module, and the westward rotation of the Region 2 FAC (shown in

Figure 3) is taken into account by adding a symmetric Fourier mode of the FAC, similar to the antisymmetric one with $m = 1$, but with the corresponding current varying with longitude as $\cos\phi$ instead of $\sin\phi$. Note that this mode of FAC has the same type of dawn-dusk symmetry/antisymmetry as the "e-modes" of the field from the equatorial currents given by equation (17).

[25] Similarly to all other magnetospheric field sources, the field $\mathbf{B}'_{FAC}$ should also be confined within the magnetopause and, hence, must be complemented by a corresponding shielding field. As in T02a (the reader is referred to that work for more details), we represented that field by a set of box harmonics having a generic form

$$u_{ik} \sim \exp\left[x(p_i^{-2} + q_k^{-2})]\right)\begin{Bmatrix} \cos(y/p_i) \\ \sin(y/p_i) \end{Bmatrix}\begin{Bmatrix} \cos(z/q_k) \\ \sin(z/q_k) \end{Bmatrix}$$

These harmonics were used for the shielding of both antisymmetric and symmetric terms in the FAC field, with the choice between sin and cos based in each case on the required parity of the magnetic field components.

4. Data Used in This Study

[26] A principal goal of this work was to develop a modeling tool, capable of deriving from the data as much as possible information on the large-scale magnetospheric structure. The size of the database is a critical factor in such studies, so we made every effort to maximize the amount of available data by including observations from new missions and expanding the previously existing sets.

4.1. Geotail Data

[27] The 13-year set of Geotail magnetometer data used in this study included more than 10 years of observations in the near tail at $10 \leq R \leq 30\ R_E$. Owing to the low inclination of Geotail, it provided a perfect coverage of the plasma sheet and adjacent tail lobe area. A comprehensive overview of the spacecraft orbit and the instrument can be found elsewhere [*Nishida*, 1994; *Kokubun et al.*, 1994]. The original data with 1-min resolution were first filtered to remove bad records and then corrected for a systematic offset in the B_z component, using high-resolution 3-s data from Geotail solar wind intervals and a variant of the Davis-Smith method [*Davis and Smith*, 1968; *Belcher*, 1973]. The corrected data were averaged over 5-min intervals and subject to a visual screen-by-screen inspection to remove the data taken outside the magnetosphere, identified with help of concurrent key parameter plasma data.

[28] With respect to the time averaging, one should realize that the effective time resolution of the models of this kind is unlikely to exceed the natural limit, corresponding to the characteristic response time of the large-scale tail current to the solar wind driving. Based on the estimates of relevant timescales, such as the typical transit time of the solar wind flow around the near magnetosphere (5–10 min) plus a characteristic time of the earthward convection in the tail (of the same order), that limit can be roughly assessed as ~15 min. The magnetopause currents respond more quickly to the solar wind pressure, but the principal factor here is the traveltime of fast magnetosonic waves across the

magnetosphere, and crude order-of-magnitude estimates of that time yield the values of at least $3-5$ min or more. Finally, in most cases the timing of the solar wind variations at Earth's orbit based on L1 point data cannot be made with the accuracy better than 5 min, and in the most interesting cases with interacting solar wind streams, shock waves, and magnetic clouds, the accuracy may be even lower. With these arguments in mind, we further averaged the Geotail field data over 15-min intervals, and that length of the averaging interval was adopted as standard for all other spacecraft, except for low-altitude orbit segments of Polar (more details below). Geotail magnetospheric data set included 135,446 15-min averages (about 12% of the total). As a general comment that refers not only to Geotail data but also to those from other spacecraft, not all of them were actually used in the modeling runs, because of incomplete coverage of the data by concurrent solar wind and IMF observations.

4.2. Cluster Data

[29] A new resource of magnetometer data, not yet tapped in our previous modeling studies, was the Cluster data archive at NSSDC CDAWEB. The original data also came with 1-min resolution and were processed using basically the same procedures as for Geotail. In order to more accurately identify the magnetopause crossings, we used the data on the proton bulk flow speed obtained by the Cluster Ion Spectrometer (CIS) [*Reme et al.*, 2001], available from the same online source. The data spanned the period from February 2001 to July 2005 and included in total 65,755 15-min averages, spatially distributed at significantly higher latitudes than the Geotail data and covering the range of radial distances between 4 and 19 R_E. More details on the orbital design of the Cluster mission and its magnetic field experiment can be found elsewhere [*Escoubet et al.*, 2001; *Balogh et al.*, 2001].

4.3. Polar Data

[30] The Polar magnetic field experiment [*Russell et al.*, 1995] was initially conceived for studying the high-latitude magnetosphere up to geocentric distances of 9 R_E. Owing to the extended lifetime of the experiment and to the slow rotation of Polar's line of apsides, the spacecraft provided complete coverage of the entire inner magnetosphere during more than 10 years of its operation. The data of Polar were prepared from 55-s averages downloaded from UCLA Polar website and covered the period from the launch (March 1996) through September 2005. All the data were visually inspected to eliminate bad records and magnetosheath/solar wind intervals, and then divided into two subsets, corresponding to high-altitude ($9.0 > R \leq 5.0\ R_E$) and low-altitude ($3.2 < R < 5.0\ R_E$) ranges of the geocentric distance. The data in the high-altitude subset were then averaged over 15-min intervals, while for the low-altitude subset we chose a shorter averaging interval of only 5 min, taking into account much higher speed of the spacecraft near Earth. Retaining the 15-min averaging in that region would result in too long orbital segments and, hence, would smear out the spatial structure of the field in the innermost magnetosphere. In total, Polar data included 212,891 data records from the high-altitude region (15-min averages) and 103,856 records from the low-altitude region (5-min aver-

ages). In terms of the number of data points, Polar contributed nearly 27% of the total in the entire database.

4.4. Geosynchronous Data

[31] Magnetic field data from synchronous orbit is a valuable resource for the magnetospheric modeling. During the last decade, most of the contribution to the synchronous data pool came from four satellites, GOES-8, GOES-9, GOES-10, and GOES-12, that provided almost continuous simultaneous monitoring of the magnetic field at two geographic longitudes, about 5 hours apart in local time. The synchronous orbit is important not only from a practical viewpoint, but also due to its unique location as a dividing line between the stable, mostly quasi-dipolar inner geomagnetic field, and much more variable outer field, often becoming tail-like during disturbed times.

[32] The synchronous data were processed using basically the same procedures as the data of other spacecraft. In contrast to purely scientific missions, the GOES satellites are not magnetically clean, and in some instances the original data were found to be contaminated by on-board sources of magnetic field. For that reason, special attention was given to visual identification and filtering out of bad data intervals, along with the magnetosheath intervals during strong compressions of the magnetopause, when the dayside boundary crossed the synchronous orbit. In total, the data of four GOES spacecraft contributed 625,481 data records with 15-min average values of the magnetic field, constituting about 54% of the total number of records in the modeling data sets. Note, however, that the apparently heavy dominance of the GOES observations was offset by applying a weighting procedure, described in more detail in section 5.2.

4.5. IMP-8 Data

[33] IMP-8 spacecraft became famous for its outstanding longevity among other space physics missions (launched in 1973, retired in 2001). Owing to its orbital parameters (a quasi-circular orbit with $R \sim 30-40\ R_E$), IMP-8 served for many years as a unique source of solar wind and IMF data, though it also contributed to several statistical studies of the magnetotail structure [e.g., *Kaymaz et al.*, 1994]. In this work, we included in our database magnetospheric magnetic field data of IMP-8 taken during $1995-2000$, when concurrent solar wind data from WIND and ACE became available. Because of a long orbital period (12.5 days) and a limited magnetospheric residence time, the number of IMP-8 data records in our database is comparatively small, only 16,317 records, that is, 1.4% of the total. Nonetheless, we consider them as an important addition to the data set, since they cover a severely underrepresented region of the distant tail ($R \sim 30-40\ R_E$) with much fewer Geotail observations.

4.6. Solar Wind and IMF Data

[34] In all our recent studies (T02, TSK03, and TS05), we used dedicated sets of the solar wind and IMF data with 5-min resolution, prepared from Wind, ACE, and IMP-8 observations. This work, in contrast, uses hourly averages from OMNI database (ftp://nssdcftp.gsfc.nasa.gov/spacecraft_data/omni/), for the following reasons. First, given the large separation between the solar wind monitors and Earth (in both the Sun-

Earth and transverse directions), using the data with 5-min resolution is not always warranted because of inevitable accumulation of large errors in the calculated propagation times between the spacecraft and the magnetosphere and additional inaccuracies, associated with lack of information on the orientation of discontinuities in the solar wind. Second, the solar wind data, especially the proton density, taken simultaneously but at different locations by different spacecraft, can differ significantly. This can even be the case for different instruments on the same spacecraft, or different methods of data processing (i.e., moments versus nonlinear analysis of distribution functions). This calls for adopting a single standard interplanetary medium data set for the space weather studies, especially in the development of quantitative magnetospheric models. The OMNI data can be viewed as a good candidate for such a standard, all the more so that a high-resolution version of the OMNI data resource is currently under construction [*King and Papitashvili*, 2005]. Finally, as discussed in section 6 below, here we focus mostly on average structures of the magnetosphere, corresponding to a set of fixed bins of interplanetary parameters and, hence, there is no need to know in great detail the dynamics of the incoming solar wind.

5.   New Elements in Data-Fitting Techniques
5.1.   Regularization of Matrix Inversion Procedures

[35]   A distinctive feature of the new approach developed in this study is the large number of elementary magnetic field sources, whose amplitudes need to be found by fitting the expansion (19) to data. The specific models discussed below have about a hundred elements describing the field of equatorial currents, each of which is shielded using a comparable number of the magnetopause field elements. As already noted in section 2.5, all the shielding coefficients are determined prior to the main procedure of fitting the model to spacecraft data and, once found, need not to be changed. In that sense, the shielding procedure is uncoupled from the main fitting and, hence, does not significantly strain the computer resources. Yet, already at the shielding stage, the use of the Gauss method of matrix inversion, employed in the earlier models, was found to result in serious problems: the range of best fit values of the shielding coefficients quickly expanded with the increase of their number, and the effect was further amplified when fitting the model to spacecraft data.

[36]   To regularize the procedure and achieve a trade-off between the accuracy of the fitting and the noise in the best fit coefficients, we employed a new technique, based on the singular value decomposition (SVD) method [*Press et al.*, 1992]. The central idea of the method is to represent the least squares normal equation matrix as a product of two ortogonal matrices and one diagonal matrix containing positive numbers, the so-called singular values. Then, in the process of the matrix inversion the smallest singular values are excluded, so that their inverse values are replaced by zeros. The number of singular values to be excluded is controlled by the tolerance parameter, which is usually the ratio between the smallest and the largest singular values to be retained. We found the SVD approach to be a very powerful tool to effectively regularize all the data fitting procedures, providing an accurate matrix inversion with reasonable amplitudes of the least squares coefficients.
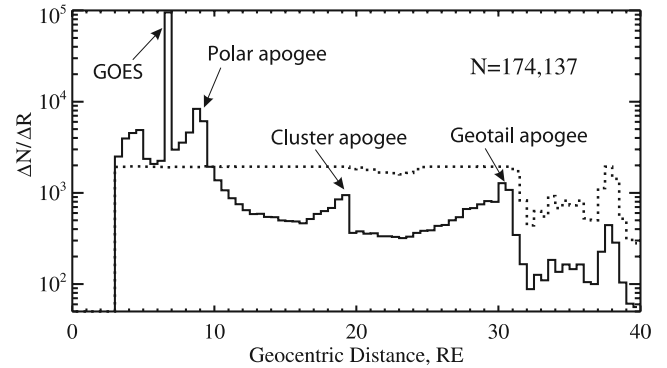

Figure 4.   Radial distribution of data points in the modeling data set, binned into 0.5 R_E intervals of the geocentric distance (solid line). Note the log scale on the vertical axis and a sharp peak at 6.6 R_E due to the GOES data. Local peaks corresponding to apogees of individual spacecraft are also indicated. Applying the weight function, inversely proportional to the radial density of the data, results in a nearly constant normalized data density (dotted line), except in the distant tail beyond 30 R_E.

5.2.   Data Weighting

[37]   Another problem arising from the increasing amount of data and the higher spatial resolution is a strong nonuniformity of the data coverage due to a limited number of spacecraft and their different orbital parameters. Figure 4 shows a histogram of the radial distribution of data in a subset corresponding to quiet conditions with Kp $\leq$ 1 (a total of 174,137 averages), binned into 0.5 R_E intervals of the geocentric distance. Even with the logarithmic scale of the vertical axis masking the large variation of the data density, it is evident that the biggest portion of data is confined within $R \leq 10$, and there is a strong disparity between the relatively sparse population of Geotail and Cluster data points in the midtail region and much denser coverage of the inner magnetosphere by Polar and GOES, the latter's contribution being confined to a narrow range of GSM latitudes and a single value of the synchronous radial distance, manifested by a sharp peak at $R = 6.6$ R_E in the plot. The secondary peaks correspond to the boundary between the regions with 5- and 15-min averaging of Polar data (at $R \approx 5$) and to the apogees of Polar, Cluster, and Geotail ($R \approx 9$, $R \approx 19$, and $R \approx 30$, respectively), where the spacecraft move most slowly and hence collect the largest amount of data. In more quantitative terms, the interval $3 \leq R \leq 10$ R_E contains 83.5% of all data points, of which 64.5% belong to the GOES data at $R = 6.6$ R_E. In contrast, the intervals $10 \leq R \leq 20$ R_E, $20 \leq R \leq 30$ R_E, and $30 \leq R \leq 40$ R_E yield only 7.7, 5.5, and 3.1% of all data, respectively.

[38]   In this situation, using the unnormalized data in the least squares fitting might result in a significant bias of the reconstructed field in the underpopulated magnetotail. To avoid that, we introduced a weighting procedure, in which the weight W was calculated as a function of the radial distance R in the following way. The entire range of the radial distance containing the data was binned into 0.5 R_E intervals, and each bin was assigned a partial weight $W_i = \langle \Delta N \rangle / \max\{0.2 \langle \Delta N \rangle, \Delta N_i\}$, where ΔN_i is the number of

data points in the ith bin and $\langle \Delta N \rangle$ is the average number per bin over the entire set. To avoid excessively large weights for severely underpopulated bins with too little data points, a lower limit was set on their number, so that if ΔN_i dropped below 20% of the average, the weight W_i was capped from above, not to exceed 5.0. The normalized radial distribution of the data density obtained by multiplying $\Delta N / \Delta R$ by W_i is shown in Figure 4 by dotted line. The normalization effectively levels the data distribution everywhere, except in the distant tail beyond Geotail's apogee, where it falls off because of too small number of observations and the capping condition.

6. Results

[39] In this section we present results of fitting the new model to several subsets of data, corresponding to different magnetospheric conditions, interplanetary parameters, and for the main and recovery storm phases. It should be emphasized that the primary goal of this work was to demonstrate the viability of the method, rather than to describe one more ready-to-use "black-box" model. In the previous models each mathematical module corresponded to a separate spatially localized magnetospheric current system, which made it physically sensible to parameterize them either by concurrent values of the solar wind parameters (as in T96), or using even more sophisticated input in the form of variables that took into account the previous history of the solar wind driving conditions (in T02 and TS05). In the present approach, by contrast, each term in the expansion (19) contains oscillating functions of the radial distance ρ and of the azimuthal angle ϕ and, in this sense, is analogous to an individual harmonic in a Fourier series. Therefore the expansion terms no longer represent separate current systems (each with its own response to the external input) but overlap each other and extend into the regions with completely different physics and response to interplanetary driving (for example, the inner ring current on the one hand, and midtail on the other). This presents a problem still awaiting a solution and relegated for future studies; in this work we resort to the old binning method, in which the data are sorted out into separate intervals of the external parameters and, based on those subsets, a family of corresponding magnetic field structures is derived, with the spatial resolution determined by the number of terms in equation (19). In other words, here we sacrifice the dynamics for the sake of getting a clearer spatial picture. In a sense, this resembles the uncertainty principle of quantum mechanics, which puts a limit on our ability to accurately measure both the position of an object in space and its momentum.

6.1. Binning by Kp Index

[40] The first set of the least squares fitting runs was made for a sequence of bins of the geomagnetic activity Kp index, as in the old TU82, T87, and T89 models. In this case the summation upper limits in equation (19) were chosen equal to $M = 4$ and $N = 5$. It should be noted that we did not impose any restrictions on the range of the solar wind dynamic pressure P_{dyn} in the data subsets and, since that parameter is of primary importance in controlling the strength of the global magnetotail magnetic field [e.g., *Tsyganenko*, 2000b], it had to be somehow included in the model. To that end, we

modified the expansion (19) by representing each of the coefficients $a_n^{(s)}$, $a_{mn}^{(o)}$, and $a_{mn}^{(e)}$, as binomials having the form $a_0 + a_1 \sqrt{P_{dyn}}$. This modification doubled the number of unknown coefficients and thus brought their total number in equation (19) up to 90. The model FAC contributed four more coefficients, including the first and second antisymmetric Fourier modes for the Region 1 system, as well as antisymmetric and symmetric principal modes for Region 2.

[41] Finally, we also added a term, corresponding to a uniform magnetic field along the z_{GSM} axis, to take into account the so-called "penetration" (or "interconnection") magnetic field, similar to that entering in the T96, T02, and TS05 approximations. In those models, the penetration field was a priori assumed to be proportional and, hence, directly controlled by the perpendicular component of the concurrent IMF. The degree of that control was defined by a proportionality factor derived from the data, and its best fit value varied between the models from 0.4 to 0.8. In this study we assumed a simpler version of the interconnection field, derived from a binned data subset just as a vector $\delta B_z \mathbf{e}_z$ in the Z direction. As discussed below, adding this term to the model resulted in a tangible improvement of the model's figure of merit and, most interesting, revealed a strong and stable correlation between δB_z and the average IMF B_z.

[42] Figure 5 shows equatorial distributions of the external part ΔB_z of the magnetospheric magnetic field (i.e., without the contribution from the Earth's sources) for four intervals of the Kp index, from the most quiet (Kp = 0, top left) to the most disturbed (Kp from 6 to 7+, bottom right). The plots correspond to zero tilt of the geodipole and faithfully reproduce all the main features of the equatorial magnetosphere, a compressed field on the dayside, a depression in the inner region, and an extended area of a generally weak field in the near tail. As the Kp index grows, so does the average ram pressure of the solar wind, which is manifested in the progressive compression of the magnetopause. Another feature clearly seen in the panels is a steady decrease of the magnetic field in the inner magnetosphere, with the largest effect on the nightside. In the most disturbed case, the depression greatly expands outwards and its center shifts toward the duskside, manifesting the development of a storm-time partial ring current. In the same panel, one can also see two local positive peaks of ΔB_z in the dawn and dusk sectors of the near tail. Their origin is not clear, but it should be kept in mind that binning the data by the Kp index inevitably results in a mixture of physically different states of the magnetosphere, making it hard to interpret details of the model field and distinguish them from artifacts.

6.2. Binning by the IMF B_z

[43] In the next set of plots we demonstrate the effect of the IMF conditions on the equatorial field. To achieve a better spatial resolution, here we used a longer expansion (19) with $M = 6$ and $N = 8$. The number of unknown coefficients in this case rose to 208. As before, four more coefficients came from four FAC modules, and one more from the "penetration" term. Therefore the total number of unknown coefficients in this version was 213. As said before, using the SVD method made it possible to effectively regularize the problem; in this regard, special attention was also paid to the optimal choice of the binning intervals of the
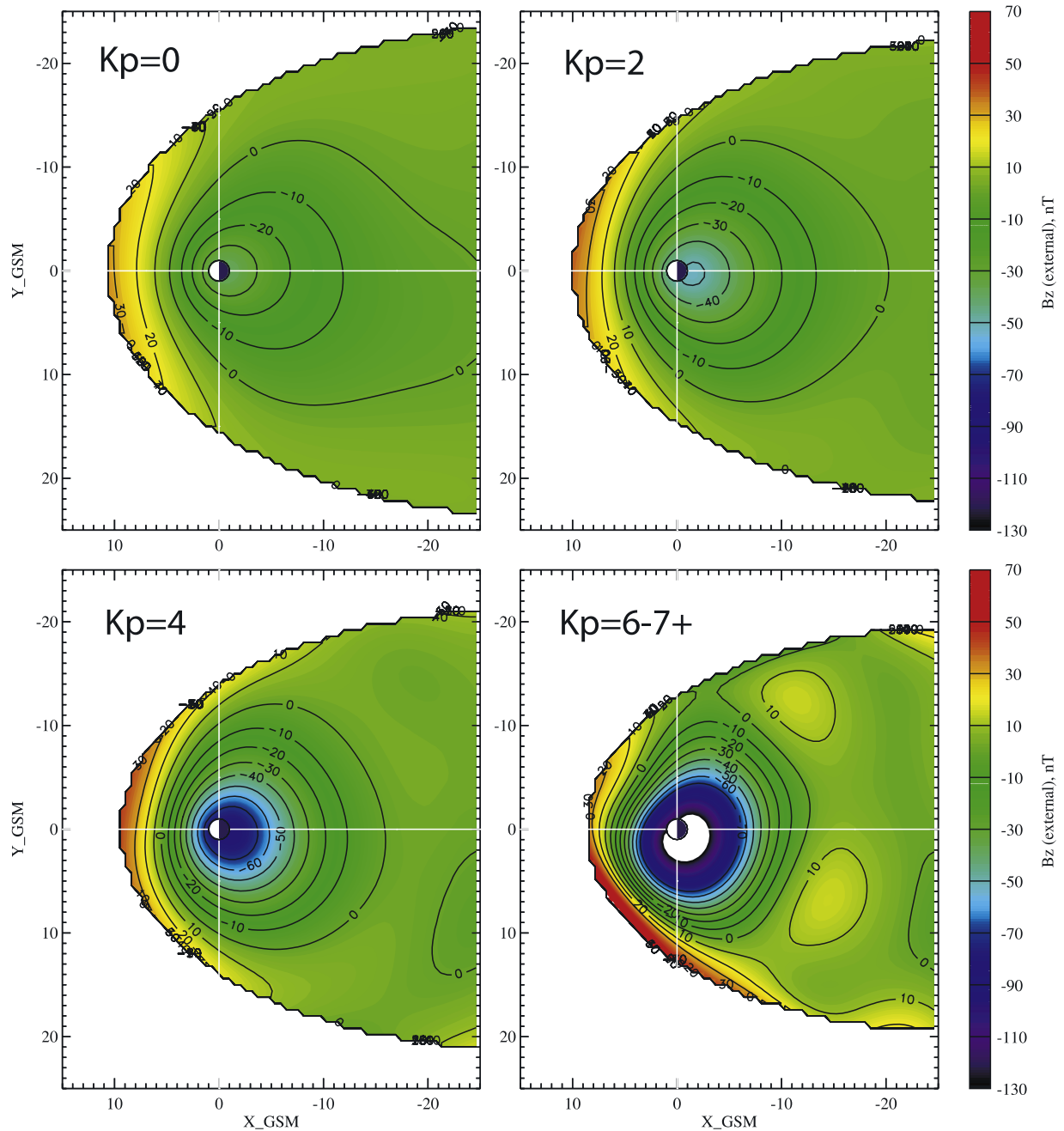
Figure 5. Color-coded distribution of B_z component of the external model field (without Earth's contribution) in the equatorial plane, for four intervals of Kp index: Kp = 0 (top left), Kp = 2 (top right), Kp = 4 (bottom left), and Kp from 6 to 7+ (bottom right).

IMF B_z, having in mind that too small subsets could result in a stronger noise and artificial features in the model field. Even though the model allowed to explicitly take into account the IMF B_y-related twisting of the magnetotail by a suitable field deformation [*Tsyganenko*, 1998], we minimized that effect by choosing only data records with IMF $|B_y| < |B_z|$. In order to more clearly resolve the effects of the IMF, its B_z component was also required to stay within a specific bin both during the current and preceding hour. Finally, in the case of positive IMF B_z an additional restriction was also imposed on the Dst index, namely, that Dst ≥ -20, with the purpose to eliminate intervals corresponding to storm recovery phases. With all

the above limitations and precautions, the data were binned into 11 intervals of the IMF B_z, with typical numbers of records in individual subsets varying in the range from ~6,000 to ~15,000.

[44] Figure 6 displays plots of the magnetospheric equatorial ΔB_z for four selected intervals of the IMF B_z, in the same format as in Figure 5. A striking effect, evident in the case of a large positive IMF B_z (top left panel) is a significant increase of the magnetic field near the magnetopause, extending over a large area and especially pronounced on the dawn side. This feature was found to be stable, in the sense that we also obtained it in other realizations of the
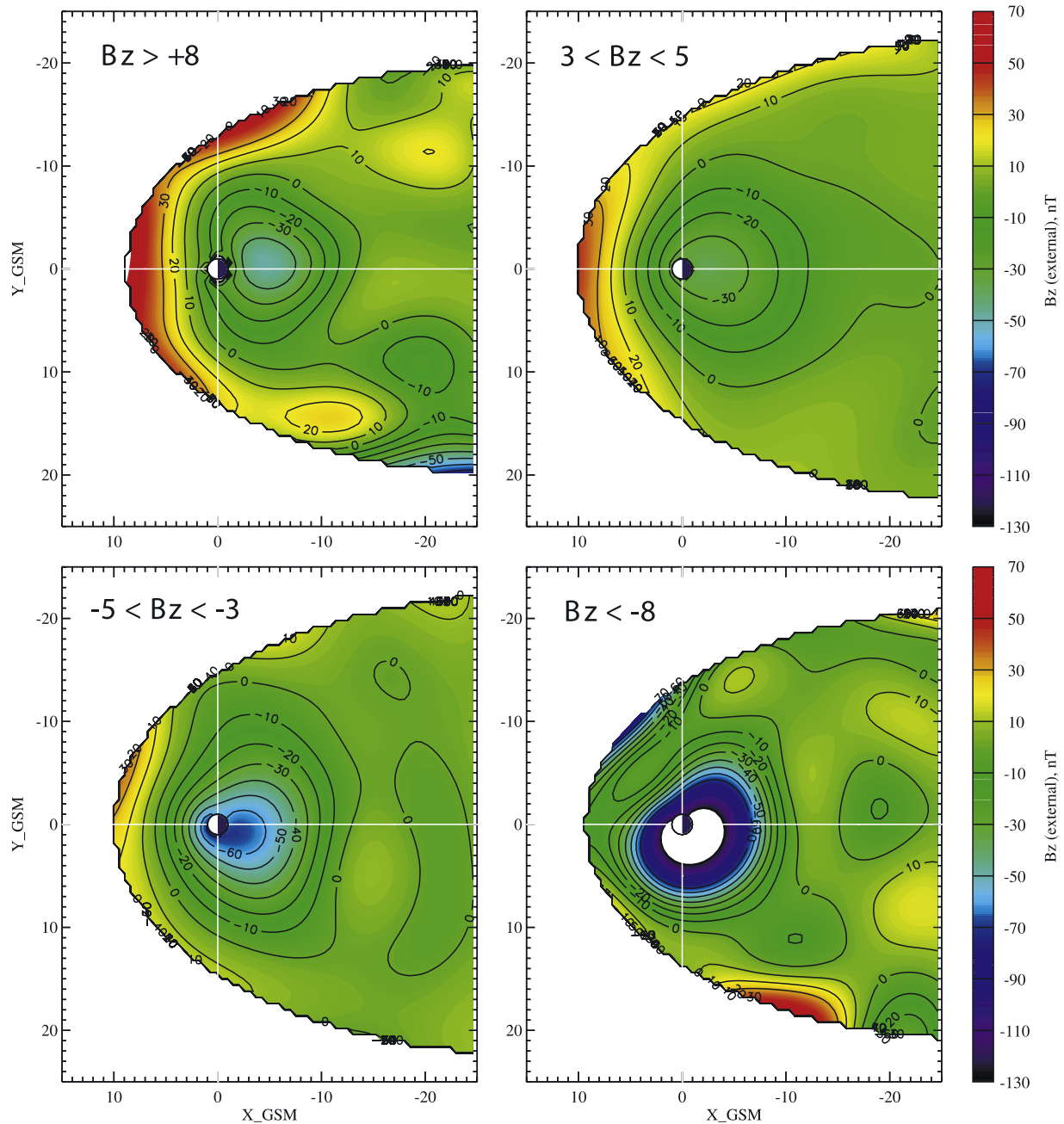
Figure 6. Same as in Figure 5, but for four intervals of IMF B_z: $B_z > +8$ nT (top left), $3 \geq B_z < 5$ (top right), $-5 \geq B_z < -3$ (bottom left), and $B_z < -8$ (bottom right).

model with a different degree of the spatial resolution and, hence, it should be treated as a real effect. Its plausible interpretation is the pile-up at the dayside magnetopause of the newly closed magnetic flux tubes, reconnected poleward from the cusps, and their subsequent tailward flow in the LLBL [*Song and Russell*, 1992; *Lavraud et al.*, 2005, 2006, and references therein]. This process is opposite to the erosion of the subsolar magnetosphere during the times of southward IMF (see below).

[45] As for the dawn-dusk asymmetry, a possible physical cause could be the asymmetry in the magnetosheath conditions, with larger particle densities (and, hence, elevated values of the frozen-in B) on the dawn side. Such an asym-metry was found [*Paularena et al.*, 2001] in IMP-8 observations of the proton density at $X \leq -10$ R_E, made near solar maximum. A similar strong dawn-dusk asymmetry was also found by *Nemecek et al.* [2002] at more sunward locations ($-10 \leq X \leq 5$ R_E) using Interball data. It remains unclear, whether this is related to asymmetries due to the spiral structure of the IMF, but in any case the question extends beyond the scope of our study.

[46] In the opposite case of negative IMF B_z (two bottom panels), one clearly sees a depression in the inner magnetosphere, dramatically expanding, growing in magnitude, and shifting duskward in the extreme case with IMF $B_z < -8$ (right). The latter plot largely resembles the one for
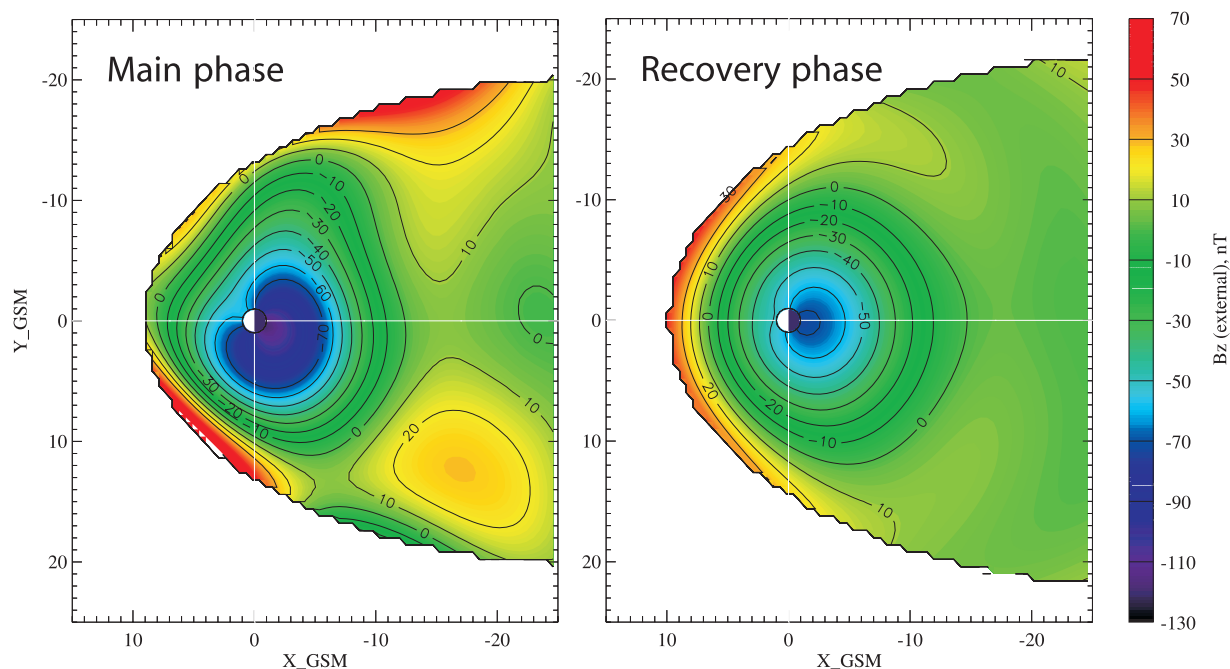
Figure 7. Same as in Figure 6, but for the main (left) and recovery (right) phases of a moderate storm.

Kp = 6–7+ in Figure 5. However, there is a significant and interesting difference: whereas the Kp-based plot included the area of strong compression of the field near the dayside magnetopause with $\Delta B_z \sim 30$ nT at the subsolar point, there is no such compression in the case of strongly negative IMF B_z in Figure 6. Moreover, here $\Delta B_z \sim -10$ nT, so that the field is actually depressed. This is the well-known effect of the erosion of the dayside magnetosphere [e.g., *Sibeck*, 1994; *Muehlbachler et al.*, 2005], associated with reconnection and strong field-aligned currents.

6.3. Main and Recovery Storm Phases

[47] In the final set of experiments, we tested the new model for its capability to replicate specific phases of a magnetic storm. To that end, a subset of data was created by selecting a set of storms of moderate magnitude, with the peak Dst in the range between −125 and −50 nT. The set covered the decade from January 1995 to December 2005 and included data for 134 events. The main and recovery phase periods were selected visually using plots of the Dst index, and the obtained lists of intervals were used for the selection of corresponding spacecraft data in the magnetosphere. In total, the main and recovery phase sets included 9,848 and 49,772 data records, respectively; the larger size of the recovery set reflects its much longer average duration, in comparison with the main phase. Figure 7 shows the obtained equatorial ΔB_z for these two cases, in the same format as in the previous plots. For the storm main phase conditions, even though the overall field distribution resembles that obtained for the cases of high Kp-index and the strong negative IMF B_z (bottom right panels of Figures 5 and 6, respectively), there is some difference. First, here the depth of the inner field depression is not as great as in the former two cases, presumably, because we chose only moderate storms. Second, the distant field in the dayside subsolar region is not as depressed as in the case of the

strong southward IMF and looks more like that in Figure 5 for Kp = 6–7+, although one still can see a narrow wedge-like area of depressed (eroded) ΔB_z in the prenoon sector, embedded between the regions of a strongly compressed field. Finally, in all three cases (Kp = 6–7+, IMF $B_z < -8$, and the storm main phase) there are local positive peaks of ΔB_z on the dawn and dusk sides of the near tail. The peaks are the most pronounced in the case of the storm main phase, and we have no clear explanation for that feature. In the case of the recovery phase, the ΔB_z distribution is much more regular and highly symmetric in the dawn-dusk direction.

[48] It is interesting to visualize and compare the data-based patterns of equatorial electric currents, corresponding to the magnetic field distributions in Figure 7. Figure 8 displays the vectors $\mathbf{j} \sim \nabla \times \mathbf{B}$, plotted against the color-coded background indicating the magnitude of the electric current density. One immediately notices a striking difference between the distributions for the main and recovery phases, not only in the overall magnitude of the currents, but also in the basic configuration of the current systems. In the first case, the distribution of the **j** vectors has nothing to do with the traditional notion of the azimuthally closed ring current: it rather has a "hook-like" shape with the largest magnitudes in the night and dusk sectors, but with virtually no current in the prenoon sector in the entire range of radial distances. This is in a good agreement with independent particle data at synchronous distance [*Denton et al.*, 2005], indicating a low ion pressure in the range from 08 to 13 hours MLT during the times of peak negative Dst. Another supporting evidence is given by ENA data: essentially all the storm-time images from IMAGE MENA and HENA show an absence of ion fluxes coming from the prenoon sector [e.g., *Brandt et al.*, 2002]. Finally, kinetic simulations of the ring current [e.g., *Liemohn et al.*, 2001] also
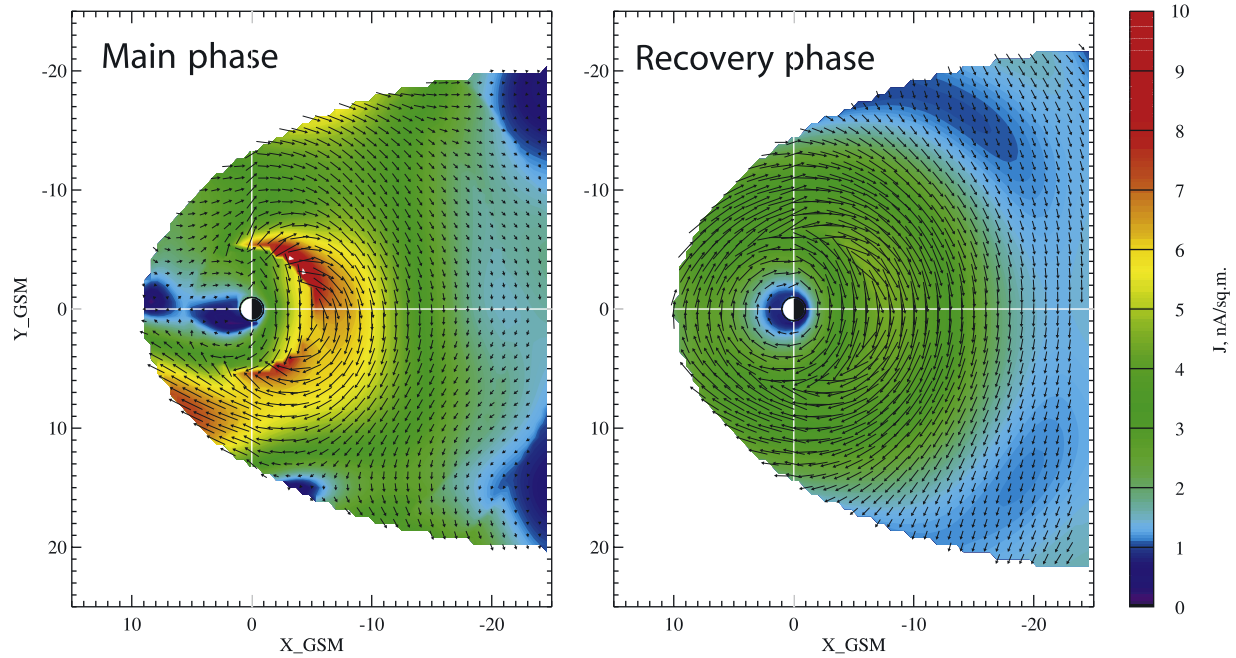
Figure 8. Distributions of the model electric current $\mathbf{j} \sim \nabla \times \mathbf{B}$ in the equatorial plane for the main (left) and recovery (right) phases of a moderate storm. At the main phase, note a dramatic increase of $\mathbf{j}$ on the nightside, fed by the inflowing/outflowing field-aligned currents in the morning/evening MLT sectors (manifested by diverging/converging $\mathbf{j}$ vectors). At the recovery phase, note a virtually axisymmetric and weaker ring current, gradually merging into the tail current sheet.

demonstrate that not much of the storm-time ring current exists in the prenoon sector.

[49] A completely different distribution of the electric currents is established during the recovery phase (right panel). In this case the model yields a roughly axisymmetric configuration, and there is virtually no distinction or transition region between the ring and tail current systems.

6.4. Field-Aligned and Equatorial Currents

[50] It is interesting to further analyze the relative role of the equatorial and field-aligned currents in the observed dawn-dusk asymmetry of the disturbed inner magnetosphere. A commonly accepted paradigm is that the storm-time duskside depression of the geomagnetic field at low latitudes is due to a PRC that develops owing to an increased convection of freshly injected particles in the evening sector [e.g., *Liemohn et al.*, 2001]. The notion of a PRC is traditionally based on a premise (dating back to *Vasyliunas* [1970]) that the azimuthally confined equatorial current closes via field-aligned currents in the ionosphere. A global model of the magnetic field associated with such a current was developed [*Tsyganenko*, 2000a] and employed in our earlier works [T02ab, TS05]. As already pointed out in section 3, in the present study the PRC is not introduced as a separate ad hoc module, but naturally emerges as an inherent part of the global three-dimensional current system, in which the flexible equatorial currents blend with the symmetric and antisymmetric components of the Region 2 FAC. Fitting such a model to data allows one to reconstruct actual magnetic configurations and to quantitatively assess individual contributions of equatorial and field-aligned currents to the storm-time field.

[51] Figure 9 shows a polar plot of the low-altitude distribution of the model FAC $j_\parallel = \mathbf{j} \cdot \mathbf{B}/B$ above the Northern Hemisphere, for the extreme case of a strong southward IMF $B_z < -8$ nT, corresponding to the right bottom panel in Figure 6. Negative/positive values (in nA/m^2) are shown by red/blue colors and correspond to outflowing/inflowing
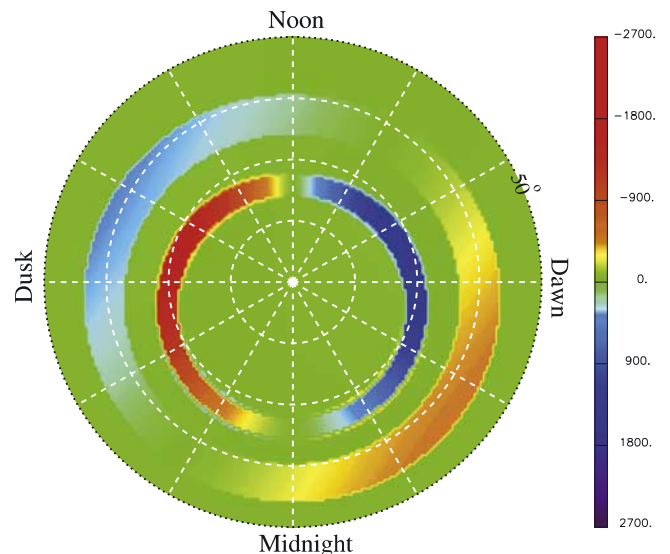

Figure 9. Distribution of Region 1 and 2 FAC at the ionospheric level, corresponding to the strong southward IMF data subset (see Figure 6, bottom right panel). Positive (blue) and negative (red) values correspond to inflowing and outflowing current, respectively.
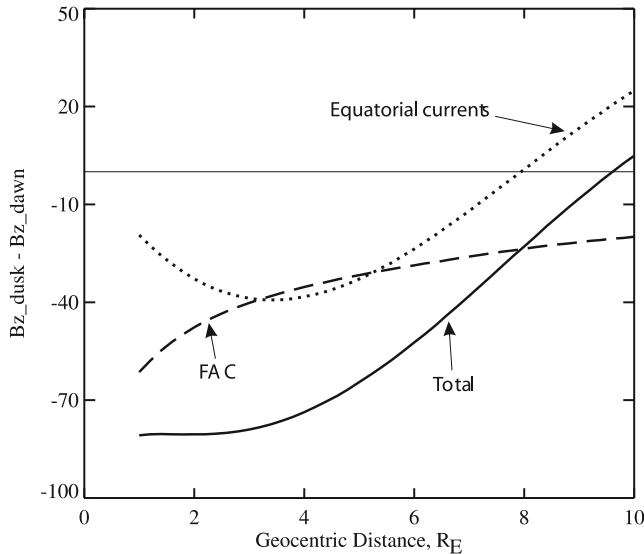
Figure 10. Illustrating the dawn-dusk asymmetry of the equatorial B_z in the case of the strong southward IMF. $B_z^{(dusk)} - B_z^{(dawn)}$ is plotted as a function of the radial distance along y_{GSM} axis. Solid, dashed, and dotted lines correspond to the total external field and to the individual contributions from the field-aligned and equatorial currents, respectively.

current, i.e., directed antiparallel/parallel to local **B** vector, respectively. Latitudinal position of the Region 1 and Region 2 zones is controlled in the model by variable nonlinear parameters defining the global scale of the corresponding three-dimensional current systems, and their best fit values were also derived from the data. As a rule, the strength and location of both systems could be determined with confidence only for southward IMF data bins, while in the case of northward IMF the location of FAC systems was found less stable and their magnitude much smaller. In the particular case, shown in Figure 9, the total inflowing Region 1 and Region 2 currents (per one hemisphere) were found equal to 2.7 and 1.9 MA, respectively. As noted above in section 3, the Region 2 system included a symmetric module, providing a day-night current and thus making it possible to take into account the azimuthal rotation of the Region 2 current and, owing to its coupling with equatorial currents, replicate the partial ring current. This effect is clearly seen in the plot: the model Region 2 zone is rotated by ~30° toward dusk, in agreement with the individual values of the total current in the antisymmetric and symmetric Region 2 modules, found equal to 1.6 and 1.0 MA, respectively.

[52] Figure 10 displays the radial variation of the dawn-dusk asymmetry of the inner magnetospheric field, calculated as the difference between the dusk and dawn model values of the equatorial B_z GSM component at the same radial distance $\rho = (X^2 + Y^2)^{1/2}$. The plots correspond to zero tilt of the geodipole and include the asymmetry of the total model field (solid line) as well as the partial contributions from the FAC and equatorial currents. As can be seen from the plot, the net asymmetry is negative almost everywhere (that is, the field at dusk is more depressed than at dawn) and reaches the largest values in the innermost region $\rho \leq 3~R_E$,

where the contribution from FAC is dominant. The contribution from equatorial currents is relatively small here, but grows with distance and becomes nearly equal to that from FAC in the interval between 3 and 5 R_E. At even larger distances the field of equatorial currents rises and turns positive at $\rho \approx 8~R_E$.

[53] It should be noted that the present model does not replicate the innermost eastward part of the ring current, caused by the positive radial gradient of the particle pressure at $\rho \leq 3~R_E$ [e.g., *Lui et al.*, 1987], for two reasons. First, our data set does not include any magnetometer data from that region, mostly because it is much more difficult to accurately separate the external part from the total field observed at small distances, due to rapidly growing internal field. Second, even with the upper limit in equation (19) as high as $N = 8$, the shortest radial wavelength in our model equals 2.5 R_E, which means that, even if the low-altitude data are available, the smaller-scale features would still remain undetected by the present version of the code. The above boils down to a rather trivial statement: to obtain a more accurate description of the inner field, one needs to increase the spatial resolution of the model (which is the simplest task) and add new data from the innermost magnetosphere (a harder problem). This can be viewed as an interesting and promising extension of the present work for the future.

6.5. "Penetrating" Field Effect

[54] Another interesting feature of the model field is the dependence of the "penetration" term $\delta B_z \mathbf{e}_z$ on the IMF B_z, already mentioned in section 6. It was found that adding that term resulted in a significant (3−4%) improvement of the fit, especially in the case of a strong southward IMF. Its magnitude δB_z was also treated as an unknown model parameter and was found along with other parameters for 11 data subsets, corresponding to consecutive intervals of the IMF B_z. Figure 11 shows the variation of δB_z against IMF B_z, revealing a strong correlation between these quantities. Two features deserve to be noted. First, there is virtually no difference in the slope of the curve between the positive and negative IMF B_z, which one might expect based on the notion of the magnetosphere as a "rectifier" that selectively responds to opposite polarities of the IMF B_z. Second, the plot has a small negative intercept at IMF $B_z = 0$, equal to ~ -2 nT, which would make it more difficult to interpret the
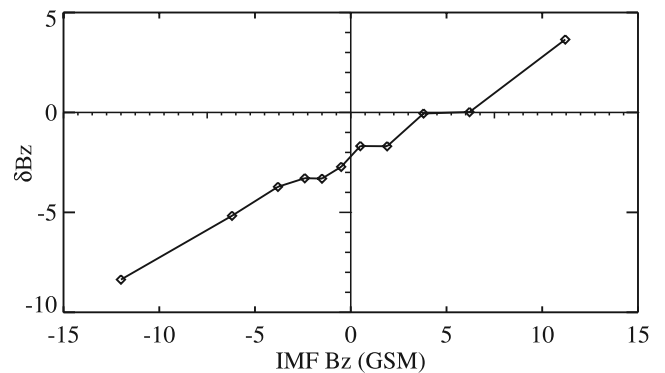

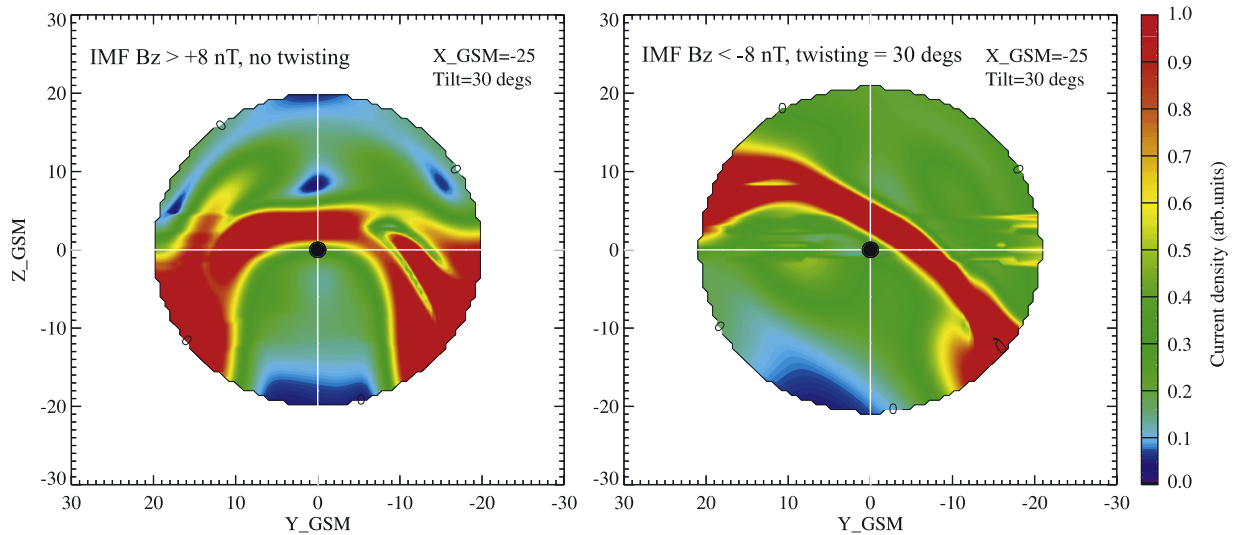**Figure 11.** The best fit "penetrating" field as a function of the IMF B_z.

Figure 12. Illustrating the tilt angle and twisting effects in the cross-section of the model magnetotail at $x_{GSM} = -25\ R_E$. (left) Strongly positive IMF B_z without twisting and (right) strongly negative IMF B_z with a twist angle 30°, corresponding to a strong and positive IMF B_y. Note a much larger warping of the current sheet in the former case.

field δB_z as a penetrated IMF, since in that case one would run into a paradoxical conclusion that positive IMF B_z penetrates in the magnetosphere as a negative δB_z. In our opinion, the easiest interpretation of this term is related to the fact that our magnetopause model does not depend on the IMF B_z, but responds only to the solar wind dynamic pressure. In actuality, the average magnetopause significantly changes its shape with the varying IMF B_z [*Shue et al.*, 1998], and that can be a primary factor behind the obtained dependence of δB_z on the IMF conditions. Introducing the variable shape of the model magnetopause still remains a major challenge in the empirical modeling, to be resolved in a future work.

6.6. Effects of the Dipole Tilt and IMF B_y on the Model Tail Current

[55]   Seasonal and diurnal variations of the Earth's dipole tilt angle Ψ with respect to the $X = 0$ plane result in a periodic transverse motion and large-scale deformation of the tail current sheet. This effect has been known since long ago [*Russell*, 1972]; the most recent quantitative model providing the shape of the tail current sheet as a function of Ψ and concurrent interplanetary parameters was devised by *Tsyganenko and Fairfield* [2004]. As shown in that work and in an earlier study [*Tsyganenko*, 1998], the net deformation of the originally planar current sheet can be represented as a superposition of bending in the X-Z plane, warping in the Y-Z plane, and twisting around the x axis. The former two deformations are due to the dipole tilt, while the latter one is associated with the IMF B_y component. A complete quantitative description of the model field deformations needed to incorporate these effects was given in T02a and in the above-cited papers. The present work uses essentially the same procedure and, to save page space, we refer the reader to the above works. Figure 12 displays the shape of the deformed model current sheet for the dipole tilt angle $\Psi = 30°$ and two opposite polarities of the IMF B_z: strong and positive/negative in the left/right panels, respec-

tively. To illustrate the IMF B_y-related deformation, a clockwise twisting by the angle 30° was added in the right panel. Our goal here was to demonstrate the geometry of the deformation, rather than the absolute magnitude of the current. For that reason, the color scale for the current volume density was saturated at the upper end and, even though the total current in the right panel is much larger, the plot does not the reproduce that difference. Regarding the shape of the current sheet, it is interesting to note a significant difference in the degree of the warping: in the case of IMF $B_z < -8$ the current sheet is much closer to a planar one, than in the case $B_z > +8$. This agrees well with our earlier conclusion [*Tsyganenko and Fairfield*, 2004], that under southward/northward IMF conditions the tail current sheet becomes more "rigid/elastic" with respect to the tilt-induced deformations.

7.   Summary and Outlook

[56]   In this paper we introduced a new method of reconstructing the global geomagnetic field from spacecraft data, using a high-resolution extensible approximation for the field of equatorial currents. The model naturally and flexibly couples the equatorial and field-aligned currents and thus makes it possible to represent with any desired resolution global distributions of the geomagnetic field for different conditions in the solar wind and in the magnetosphere, provided a sufficient coverage by spacecraft data is available. A new database of spacecraft magnetometer data has also been compiled, and the high-resolution model has been calibrated against various subsets of that database. The obtained detailed maps of the magnetic field revealed all the principal elements of the magnetospheric structure, their dependence on the interplanetary conditions, and the basic changes associated with principal phases of a magnetic storm. Specifically, the model reveals the following features: (1) compressed field on the dayside, growing in magnitude with increasing solar wind pressure; (2) strong erosion of the

field in the subsolar region during the times of large southward IMF, driving the storm main phase; (3) depression of the inner magnetospheric field, whose depth and dawn-dusk asymmetry dramatically grow during storm-time periods; (4) extended region of weak equatorial field in the near tail, increasing toward the tail's flanks, especially for strong northward IMF conditions; (5) strong correlation of the "penetrating" δB_z with the concurrent IMF B_z; (6) strong increase of the current in the postmidnight and evening sectors at the storm main phase, accompanied by its dramatic reduction in the entire prenoon sector and resulting in a hooklike shape of the overall pattern of the storm-time equatorial current; (7) fairly broad and virtually axisymmetric equatorial current for the storm recovery phase (in sharp contrast with 6), without any significant distinction between the ring and tail current systems.

[57] The presented method can be likened to making a snapshot of the magnetosphere with a camera, with a similar trade-off problem as in the photography: to get a good image, one needs a long enough exposure (in our case, a sufficiently dense coverage of the magnetosphere by the data). On the other hand, too long an exposure may result in smearing and loss of important details because of the finite rate of the object's temporal evolution. A perfect source of data to be used with this technique would be a Constellation-class mission [*Angelopoulos et al.*, 1998], intended to provide dense grids of observation samples for any given time interval. Nevertheless, as demonstrated in this study, even with already available sets of data from many spacecraft and rather simple data-binning procedures it is possible to discern basic features of the magnetospheric structure/dynamics, as well as new interesting effects, such as the significant increase of the near-magnetopause field during strong northward IMF conditions. Even without the Constellation-level data resource, our method can significantly improve the spatial resolution of the models like T02 and TS05. A promising approach in this regard is to advance the conventional data binning procedures by using modern techniques of time series processing, such as the nearest-neighbors and time delay embedding, successfully employed in the nonlinear modeling and prediction of global magnetospheric parameters [e.g., *Vassiliadis et al.*, 1995; *Ukhorskiy et al.*, 2004]. That would make it possible to fully implement our new technique in the empirical models and bring them to the level of forecasting tools.

References

Angelopoulos, V., C. W. Carlson, D. W. Curtis, P. Harvey, R. P. Lin, F. S. Mozer, D. H. Pankow, J. Raeder, and C. T. Russell (1998), On the necessity and feasibility of an equatorial Magnetospheric Constellation, in *Science Closure and Enabling Technologies for Constellation Class Missions*, edited by V. Angelopoulos and P. V. Panetta, pp. 14–21, UC Berkeley, Calif.

Balogh, A., et al. (2001), The Cluster magnetic field investigation: Overview of in-flight performance and initial results, *Ann. Geophys.*, *19*, 1207.

Belcher, J. A. (1973), A variation of the Davis-Smith method for in-flight determination of spacecraft magnetic fields, *J. Geophys. Res.*, *78*, 6480.

Brandt, P. C:son, S. Ohtani, D. G. Mitchell, M.-C. Fok, E. C. Roelof, and R. Demajistre (2002), Global ENA observations of the storm main-phase ring current: Implications for skewed electric fields in the inner magnetosphere, *Geophys. Res. Lett.*, *29*(20), 1954, doi:10.1029/2002GL015160.

Davis, L., Jr., and E. J. Smith (1968), *Eos Trans. AGU*, *49*, 257.

Denton, M. H., V. K. Jordanova, M. G. Henderson, R. M. Skoug, M. F. Thomsen, C. J. Pollock, S. Zaharia, and H. O. Funsten (2005), Storm-time plasma signatures observed by IMAGE/MENA and comparison with a global physics-based model, *Geophys. Res. Lett.*, *32*, L17102, doi:10.1029/2005GL023353.

Escoubet, C. P., M. Fehringer, and M. Goldstein (2001), The Cluster mission, *Ann. Geophys.*, *19*, 1197.

Fairfield, D. H. (1986), The magnetic field of the equatorial magnetotail from 10 to 40 Re, *J. Geophys. Res.*, *91*, 4238.

Kaymaz, Z., G. L. Siscoe, N. A. Tsyganenko, and R. P. Lepping (1994), Magnetotail views at 33RE: IMP 8 magnetometer observations, *J. Geophys. Res.*, *99*, 8705.

King, J. H., and N. E. Papitashvili (2005), Solar wind spatial scales in and comparisons of hourly Wind and ACE plasma and magnetic field data, *J. Geophys. Res.*, *110*, A02104, doi:10.1029/2004JA010649.

Kokubun, S., T. Yamamoto, M. H. Acuna, K. Hayashi, K. Shiokawa, and H. Kawano (1994), The Geotail magnetic field experiment, *J. Geomagn. Geoelectr.*, *46*, 7.

Lavraud, B., M. F. Thomsen, M. G. G. T. Taylor, Y. L. Wang, T. D. Phan, S. J. Schwartz, R. C. Elphic, A. Fazakerley, H. Reme, and A. Balogh (2005), Characteristics of the magnetosheath electron boundary layer under northward IMF: Implications for high-latitude reconnection, *J. Geophys. Res.*, *110*, A06209, doi:10.1029/2004JA010808.

Lavraud, B., M. F. Thomsen, B. Lefebvre, S. J. Schwartz, K. Seki, T. D. Phan, Y. L. Wang, A. Fazakerley, H. Reme, and A. Balogh (2006), Evidence for newly closed magnetosheath field lines at the dayside magnetopause under northward IMF, *J. Geophys. Res.*, *111*(A5), A05211, doi:10.1029/2005JA011266.

Liemohn, M. W., J. U. Kozyra, M. F. Thomsen, J. L. Roeder, G. Lu, J. E. Borovsky, and T. E. Cayton (2001), Dominant role of the asymmetric ring current in producing the stormtime Dst, *J. Geophys. Res.*, *106*, 10,883.

Lui, A. T. Y., R. W. McEntire, and S. M. Krimigis (1987), Evolution of the ring current during two geomagnetic storms, *J. Geophys. Res.*, *92*, 7459.

Moon, P., and D. E. Spencer (1971), *Field Theory Handbook*, 2nd ed., Springer, New York.

Muehlbachler, S., C. J. Farrugia, J. Raeder, H. K. Biernat, and R. B. Torbert (2005), A statistical investigation of dayside magnetosphere erosion showing saturation of response, *J. Geophys. Res.*, *110*, A11207, doi:10.1029/2005JA011177.

Nemecek, Z., J. Safrankova, G. N. Zastenker, P. Pisoft, and K. I. Paularena (2002), Spatial distribution of the magnetosheath ion flux, *Adv. Space Res.*, *30*(12), 2751.

Nishida, A. (1994), The Geotail mission, *Geophys. Res. Lett.*, *21*, 2871.

Paularena, K. I., J. D. Richardson, M. A. Kolpak, C. R. Jackson, and G. L. Siscoe (2001), A dawn-dusk asymmetry in Earth's magnetosheath, *J. Geophys. Res.*, *106*, 25,377.

Press, W. H., S. A. Teukolsky, W. T. Vetterling, and B. P. Flannery (1992), *Numerical Recipes*, 2nd ed., Cambridge Univ. Press, New York.

Reme, H., et al. (2001), First multispacecraft ion measurements in and near the Earth's magnetosphere with the identical Cluster ion spectrometry (CIS) experiment, *Ann. Geophys.*, *19*, 1303.

Russell, C. T. (1972), The configuration of the magnetosphere, in *Critical Problems of Magnetospheric Physics*, edited by E. R. Dyer, pp. 1–16, IUCSTP Sec., Nat. Acad. of Sci., Washington, D. C.

Russell, C. T., R. C. Snare, J. D. Means, D. Pierce, D. Dearborn, M. Larson, G. Barr, and G. Le (1995), The GGS/Polar magnetic field investigation, *Space Sci. Rev.*, *71*, 563.

Shue, J.-H., P. Song, C. T. Russell, J. T. Steinberg, J. K. Chao, G. Zastenker, O. L. Vaisberg, S. Kokubun, H. J. Singer, T. R. Detman, and H. Kawano (1998), Magnetopause location under extreme solar wind conditions, *J. Geophys. Res.*, *103*, 17,691.

Sibeck, D. G. (1994), Signatures of flux erosion from the dayside magnetosphere, *J. Geophys. Res.*, *99*, 8513.

Song, P., and C. T. Russell (1992), Model of the formation of the low-latitude boundary layer for strongly northward interplanetary magnetic field, *J. Geophys. Res.*, *97*(A2), 1411.

Sotirelis, T., N. A. Tsyganenko, and D. P. Stern (1994), Method for confining the magnetic field of the cross-tail current inside the magnetopause, *J. Geophys. Res.*, *99*, 19,393.

Stern, D. P. (1987), Tail modeling in a stretched magnetosphere: 1. Methods and transformations, *J. Geophys. Res.*, *92*, 4437.

Stubbs, T. J., M. Lockwood, P. Cargill, J. Fennell, M. Grande, B. Kellett, C. Perry, and A. Rees (2001), Dawn-dusk asymmetry in particles of solar wind origin within the magnetosphere, *Ann. Geophys.*, *19*, 1.

Tsyganenko, N. A. (1989), A magnetospheric magnetic field model with a warped tail current sheet, *Planet. Space Sci.*, *37*, 5.

Tsyganenko, N. A. (1990), Quantitative models of the magnetospheric magnetic field: Methods and results, *Space Sci. Rev.*, *54*, 75.

Tsyganenko, N. A. (1991), Methods for quantitative modeling of the magnetic field from Birkeland currents, *Planet. Space Sci.*, *39*, 641.

Tsyganenko, N. A. (1995), Modeling the Earth's magnetospheric magnetic field confined within a realistic magnetopause, *J. Geophys. Res.*, *100*, 5599.

Tsyganenko, N. A. (1996), Effects of the solar wind conditions on the global magnetospheric configuration as deduced from data-based field models, in Proceedings of the ICS-3 Conference on Substorms, Eur. Space Agency Spec. Publ., ESA SP-389, 181.

Tsyganenko, N. A. (1998), Modeling of twisted/warped magnetospheric configurations using the general deformation method, *J. Geophys. Res.*, *103*, 23,551.

Tsyganenko, N. A. (2000a), Modeling the inner magnetosphere: The asymmetric ring current and Region 2 Birkeland currents revisited, *J. Geophys. Res.*, *105*, 27,739.

Tsyganenko, N. A. (2000b), Solar wind control of the tail lobe magnetic field as deduced from Geotail, AMPTE/IRM, and ISEE-2 data, *J. Geophys. Res.*, *105*(A3), 5517.

Tsyganenko, N. A. (2002a), A model of the near magnetosphere with a dawn-dusk asymmetry 1. Mathematical structure, *J. Geophys. Res.*, *107*(A8), 1179, doi:10.1029/2001JA000219.

Tsyganenko, N. A. (2002b), A model of the near magnetosphere with a dawn-dusk asymmetry 2. Parameterization and fitting to observations, *J. Geophys. Res.*, *107*(A8), 1176, doi:10.1029/2001JA000220.

Tsyganenko, N. A., and D. H. Fairfield (2004), Global shape of the magnetotail current sheet as derived from Geotail and Polar data, *J. Geophys. Res.*, *109*, A03218, doi:10.1029/2003JA010062.

Tsyganenko, N. A., and M. Peredo (1994), Analytical models of the magnetic field of disk-shaped current sheets, *J. Geophys. Res.*, *99*, 199.

Tsyganenko, N. A., and M. I. Sitnov (2005), Modeling the dynamics of the inner magnetosphere during strong geomagnetic storms, *J. Geophys. Res.*, *110*, A03208, doi:10.1029/2004JA010798.

Tsyganenko, N. A., H. J. Singer, and J. C. Kasper (2003), Storm-time distortion of the inner magnetosphere: How severe can it get?, *J. Geophys. Res.*, *108*(A5), 1209, doi:10.1029/2002JA009808.

Ukhorskiy, A. Y., M. I. Sitnov, A. S. Sharma, and K. Papadopoulos (2004), Global and multi-scale features of solar wind-magnetosphere coupling: From modeling to forecasting, *Geophys. Res. Lett.*, *31*, L08802, doi:10.1029/2003GL018932.

Vassiliadis, D., A. J. Klimas, D. N. Baker, and D. A. Roberts (1995), A description of the solar wind-magnetosphere coupling based on nonlinear filters, *J. Geophys. Res.*, *100*, 3495.

Vasyliunas, V. M. (1970), Mathematical models of magnetospheric convection and its coupling to the ionosphere, in *Particles and Fields in the Magnetosphere*, edited by B. M. McCormac, pp. 60–71, Springer, New York.

_____

M. I. Sitnov, Institute for Research in Electronics and Applied Physics, University of Maryland, College Park, MD 20742, USA. (sitnov@umd.edu)

N. A. Tsyganenko, Universities Space Research Association, Code 674, Space Weather Laboratory, NASA Goddard Space Flight Center, Greenbelt, MD 20771, USA. (nikolai.tsyganenko@gsfc.nasa.gov)